

REPORT DOCUMENTATION PAGE

1a. REPORT SECURITY CLASSIFICATION
Unclassified

1b. RESTRICTIVE MARKINGS

3. DISTRIBUTION / AVAILABILITY OF REPORT
Approved for public release;
distribution unlimited.

AD-A232 703

5. MONITORING ORGANIZATION REPORT NUMBER(S)
AFOSR-TR- 81-0047

6a. NAME OF PERFORMING ORGANIZATION
Research Laboratory of Electronics
Massachusetts Institute of Technology

6b. OFFICE SYMBOL
(if applicable)

7a. NAME OF MONITORING ORGANIZATION
AFOSR

6c. ADDRESS (City, State, and ZIP Code)

77 Massachusetts Avenue
Cambridge, MA 02139

7b. ADDRESS (City, State, and ZIP Code)

BLDG 410
Bolling AFB DC 20332-6448

8a. NAME OF FUNDING / SPONSORING
ORGANIZATION
A.F. Off. of Sci. Research

8b. OFFICE SYMBOL
(if applicable)
NE

9. PROCUREMENT INSTRUMENT IDENTIFICATION NUMBER

F49620-87-C-0043

8c. ADDRESS (City, State, and ZIP Code)

Building 410
Bolling Air Force Base, DC 20332

10. SOURCE OF FUNDING NUMBERS

PROGRAM
ELEMENT NO.

611025

PROJECT
NO.

2305

TASK
NO.

B2

WORK UNIT
ACCESSION NO.

11. TITLE (Include Security Classification)

Analog Processing of Optical Wavefronts Using Integrated Guided-Wave Optics

12. PERSONAL AUTHOR(S)

Dr. Robert H. Rediker

13a. TYPE OF REPORT
Final

13b. TIME COVERED
FROM 3-15-87 TO 7-31-90

14. DATE OF REPORT (Year, Month, Day)
November 30, 1990

15. PAGE COUNT
37

16. SUPPLEMENTARY NOTATION

17. COSATI CODES

FIELD	GROUP	SUB-GROUP

18. SUBJECT TERMS (Continue on reverse if necessary and identify by block number)

19. ABSTRACT (Continue on reverse if necessary and identify by block number)

Progress was made on the design and study of an integrated optical module for phase sensing and steering, also containing an efficient, tapered dielectric antenna.

DTIC
ELECTE
MAR 12 1991
S D

20. DISTRIBUTION / AVAILABILITY OF ABSTRACT

☒ UNCLASSIFIED/UNLIMITED ☒ SAME AS RPT. ☐ DTIC USERS

21. ABSTRACT SECURITY CLASSIFICATION

Unclassified

22a. NAME OF RESPONSIBLE INDIVIDUAL
Dr Howard R. Schlossberg

22b. TELEPHONE (Include Area Code)
202/767-4906

22c. OFFICE SYMBOL
NE

RESEARCH LABORATORY OF ELECTRONICS
MASSACHUSETTS INSTITUTE OF TECHNOLOGY
CAMBRIDGE, MASSACHUSETTS 02139

Analog Processing of Optical Wavefronts
Using Integrated Guided-Wave Optics
Contract # F 49620-87-C-0043

Final Report
Period Covered March 15, 1987-July 31, 1990



Accession For	
NTIS CRA&I	
DTIC TAB	
Unannounced	
Justification	
By	
Distribution/	
Availability Codes	
Dist	Avail and/or Special
A-1	

Submitted to the U.S. Air Force - Office of Scientific Research

Dr. Robert H. Rediker, Principal Investigator

November 30, 1990

91 3 06 095

Table of Contents

I.	Introduction	1
II.	The Basic Module	2
	A. Concept	2
	B. The Operation of the Basic Module	4
III.	Antenna Development	6
	A. Concept	7
	B. MBE Growth Technique	9
	C. Experimental Results	13
	D. Numerical Simulation	20
IV.	Wavefront Phase Tilt Measurement	29
	References	36

ANALOG PROCESSING OF OPTICAL WAVEFRONTS
USING INTEGRATED GUIDED-WAVE OPTICS

Final Report to the Air Force Office of Scientific Research
Contract # F49620-87-C-0043

March 15, 1987 — July 31, 1990

Robert H. Rediker

Massachusetts Institute of Technology
Department of Electrical Engineering and Computer Science
and Research Laboratory of Electronics

I. Introduction

Integrated Guided-Wave Optics has many advantages for the analog processing of optical wavefronts. These include small-size, high-speed, simplicity, reliability and reproducibility. The fabrication technique is similar to that of integrated circuits. The thrust of this program was to develop an integrated guided-wave optic system, in GaAs and GaAlAs for use at GaAs laser wavelength, to remove aberrations from a laser beam and to steer the beam. The system would in addition have the capability to appropriately phase the outputs from a multiplicity of power amplifiers or injection-locked lasers. It was also the intent of the program to design and build the optical circuits so they are compatible with on-chip electronic circuits in order to minimize the required number of off-chip leads.

The research program was proposed by MIT Research Laboratory of Electronics with part of the work being performed at MIT Lincoln Laboratory. In general, guided-wave component evaluation, analysis and understanding of optimization was performed at MIT Research Laboratory of Electronics, while the fabrication and actual optimization was performed at MIT Lincoln Laboratory.

Experiments have shown that integrated guided-wave optics can successfully be employed to measure and/or modify optical wavefronts.¹ The electrooptic material used in these experiments was Ti:LiNbO_3 . Recently, however, there have been significant advances in the use of semiconductors as the electrooptic material in which integrated optical devices are fabricated.² This program seeks to explore the fundamental issues associated with optical wavefront correction using integrated guided-wave devices in GaAlAs for use at GaAs/GaAlAs laser wavelengths.

In Section II A the concept for correction of an optical wavefront is presented and several obvious advantages of "on-chip processing" are pointed out. Section II B describes the operation of the proposed basic integrated-optics module for integrated guided-wave optics systems to do the required wavefront correction and steering. Many basic properties of guided-wave optics need to be better understood and optimized before the proposed concept can be realized in a practical manner. In the work described in this report we have focussed our attention on two integrated-optic components which have requirements, in addition to wavelength of operation, specific to the thrust of our program. In Section III we describe the design and development of a two-dimensional antenna to enhance the coupling of guided-wave optical radiation into free space. Our program requires the measurement of wavefront tilt by an interferometer in which the powers in the interferometer arms are unequal and are variable. Section IV describes such a wavefront phase tilt measuring system.

II. The Basic Module

A. Concept

The basic module proposed for wavefront correction is shown in Fig. 1. The system could contain as few as ten modules or as many modules as limited by reliability and reproducibility or other system considerations. Figure 1 is the

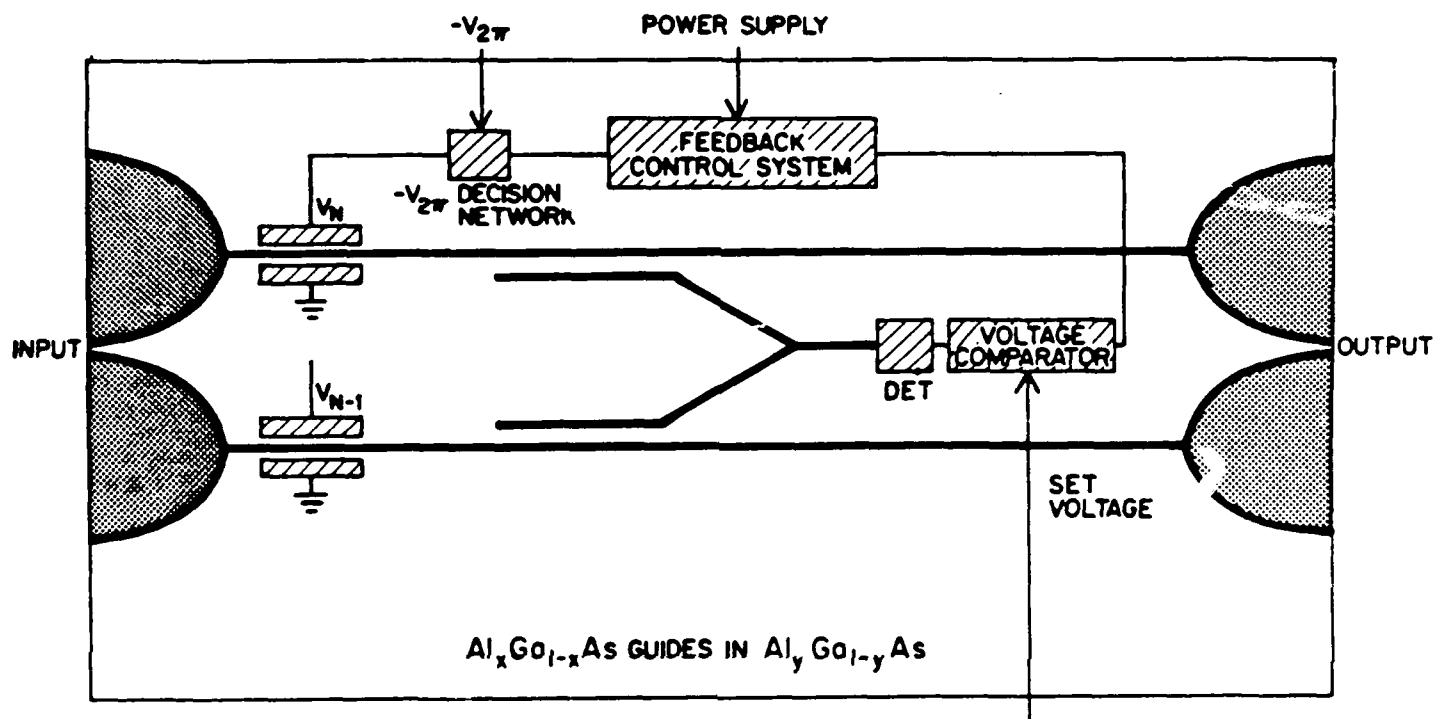


Fig. 1 The basic module for wavefront correction. In practice of the order of 10^3 modules may be appropriate for high-resolution correction. A significant advantage of the concept is the on-chip processing which reduces dramatically the number of leads required to come off the chip. The guides have a lower fraction, x , of Al in the $Al_xGa_{1-x}As$ than the fraction, y , in the substrate for dielectric confinement of the electromagnetic wave.

same as Fig. 6 in the U.S. Patent³ issued to the principal investigator, except it also includes the on-chip detector, voltage comparator and feedback control system. The advantages of this "on-chip processing" are the reduction of the number of leads that are required to come off the chip and the reduction of complexity of off-chip processing and time delays in signal transmission and processing. For example, in a system with 10^3 modules, only one control set-voltage is required (one lead). Without on-chip processing 10^3 voltages V_N need to be determined by the off-chip processor and require up to 10^3 leads to impress these voltages. It should be pointed out that there is a 2π radians (360°) ambiguity in the phase of the output from any waveguide. The voltage, V_N , need never exceed $V_{2\pi}$, the voltage across the waveguide electrodes to produce a change in the phase of 2π radians. Of course the incoming aberrated beam will be distorted by much more than 2π radians over the aperture of 10^3 modules. A second lead to the chip is required for on-chip $V_{2\pi}$ corrections to keep all V_N to correspond to phase shifts between 0 and 2π . For example if the aberration over the aperture is 50π and $V_{2\pi} = 20$ V, then without the successive $V_{2\pi}$ corrections V_N would equal 500 V, which is not feasible for many fundamental and practical reasons.

While the module shown in Fig. 1 is specific to removing aberrations in the wavefront or steering the beam, using the same basic components other figures in the aforementioned patent illustrate the focussing of the wavefront. In general, analog processing of the optical wavefront is possible with various configurations of the components illustrated in Fig. 1.

B. The Operation of the Basic Module

The operation of the basic module in Fig. 1 is as follows: The voltage V_N delays the phase of the optical wave in waveguide N by ϕ_N and the voltage V_{N-1} delays the phase of the optical wave in waveguide (N-1) by ϕ_{N-1} so that the two

waves emerge from the waveguides in phase (the aberration is removed) or at a predetermined phase (the aberration is removed and the beam is steered). Evanescent wave coupling is used to couple a small fraction δ of the power in each straight-through waveguide to the adjacent arm of the interferometer between the waveguides. For equal incident optical powers, P , incident on each waveguide and equal evanescent coupling, δ , to each interferometer arm, the optical power incident on the detector is

$$P_{\Delta\phi} = [2\delta P \cos^2 \frac{\phi_N - \phi_{N-1}}{2}] B \quad (1)$$

where B takes into account additional losses in interferometer arms such as due to the bends. When the powers P are unequal and/or the couplings δ , are unequal eq. (1) contains additional terms as is discussed in Section IV below. Also presented in Section IV are techniques to measure $(\Delta\phi = \phi_N - \phi_{N-1})$ independent of the powers P , the couplings δ and the losses taken into account by B . In integrated optics as in integrated circuits it is important for operation to be independent of individual component variations. With the appropriate set voltage V_s applied to the voltage comparator in Fig. 1 the feedback control system will set the value of V_N with respect to $V_{(N-1)}$ so that the phase shift $(\phi_N - \phi_{N-1})$ between the outputs of the two straight waveguides is zero. The details of the feedback control system are not described here, except to mention that it is a relatively straightforward system which nulls the difference between the detector output voltage and the set voltage introduced from off the chip. As part of the electronic circuit, as mentioned earlier, there is a " $V_{2\pi}$ decision network" to reduce V_N below the maximum value of the voltage $V_{2\pi}$ which produces a phase shift of 2π radians (360°). Subtracting (or adding if V_N is negative) $V_{2\pi}$ does not change the phase of the output from the straight-through waveguide.

III. Antenna Development

The first integrated optics component we are developing under this program is the adiabatic antenna shown as a horn in Fig. 1. The success of this program, and many other integrated optics programs depends on the efficient collection of incident light and the efficient emission of laser light from the semiconductor. What is desired is an adiabatic antenna (an antenna that remains single-mode and loses no energy out of this mode) with an antenna pattern in which almost all of the energy is in a highly-directional central lobe.

In addition, integrated optoelectronic circuits frequently incorporate components such as electrooptic modulators and Y-junctions that require waveguides with a small mode size for efficient device operation. When coupling into free space, however, a large mode size is desirable at the device output endface in order to obtain a highly directional far-field beam. Optical horn antennas, for example, have been used to produce a lateral increase in the size of a guided mode, thereby reducing the lateral far-field beam divergence.⁴ In our program we have addressed monolithically integrated reduced-confinement GaAlAs waveguide antennas potentially capable of increasing the size of a guided mode in both the transverse and lateral dimensions. The concept of a reduced-confinement antenna has been used at microwave frequencies since the 1940s in the dielectric "polyrod" antenna.⁵

We describe here the fabrication, operation and optimization of reduced-confinement GaAlAs tapered waveguide antennas for use in coupling to free-space radiation. These antennas, which are designed to operate at GaAs-laser wavelengths (e.g., $0.88\ \mu\text{m}$), are produced by using a novel single-step molecular-beam-epitaxy (MBE) growth technique.^{6,7} This technique allows us to grow single-mode structures in which a tapered GaAlAs waveguide film varying longitudinally in both thickness and Al concentration, and therefore refractive index, is

sandwiched between two uniform lower-index cladding layers. In these slab waveguide antennas, the transverse confinement of the guided mode is reduced near the device output endface both by decreasing the waveguide film thickness and, more importantly, by decreasing the refractive index difference between the waveguide film and cladding. Using this structure, we have demonstrated reductions of >35% in the transverse far-field beam divergence for radiation emitted from single-mode GaAlAs slab waveguides. The reduced-confinement geometry is particularly advantageous because it will permit fabrication of two-dimensional GaAlAs antenna structures capable of independently tailoring far-field beam profiles in the directions both perpendicular and parallel to the wafer surface.

The concept of a reduced-confinement tapered waveguide antenna is presented in Section III A, and the MBE growth technique that allows us to produce these monolithically integrated GaAlAs antennas is described in Section III B. The experimental performance of reduced-confinement GaAlAs slab waveguide antennas is reported in Section III C, and performance limitations of these antennas resulting from finite cladding thicknesses are also discussed. Section III D presents the results of a numerical simulation of reduced-confinement antennas in which the effects of taper length on antenna performance are investigated for two simple taper geometries. Specifically, requirements on the amplitude and phase profiles of the electric field at the antenna output are analyzed and discussed.

A. Concept

The concept of a reduced-confinement tapered waveguide antenna is illustrated in Fig. 2. The cross-sectional profile of a nontapered buried symmetric slab waveguide is shown in Fig. 2(a), in which a uniform-index waveguide film of constant thickness is sandwiched between two identical lower-index cladding layers. The fundamental guided mode propagates along the length of this structure without changing its shape. This guided mode is characterized by an effective mode width,

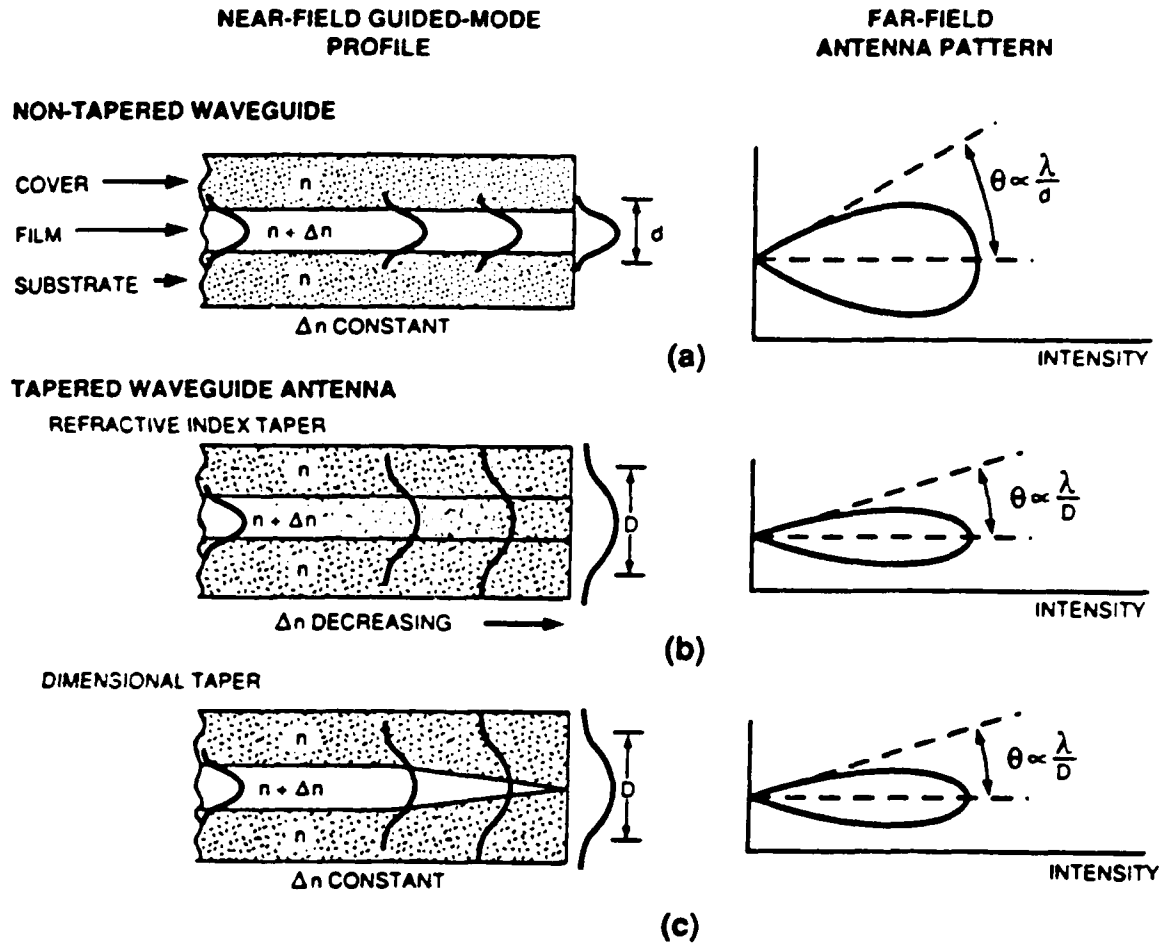


Fig. 2 The concept of a reduced-confinement tapered waveguide antenna. Guided-mode intensity profiles and far-field antenna patterns for (a) a uniform (nontapered) slab waveguide, (b) a waveguide in which the refractive index difference between the film and cladding, Δn , is reduced near the device endface, and (c) a waveguide in which the waveguide film thickness is reduced near the output endface.

denoted by d in Fig. 2(a). The effective mode width accounts for the finite penetration depth of the guided mode's evanescent tails into the surrounding cladding layers. The far-field antenna pattern for radiation emitted from the nontapered device is also shown in Fig. 2(a). Note that the far-field beam divergence is, to first order, inversely proportional to the effective width of the guided mode at the waveguide output endface.

The effects of a monolithically integrated reduced-confinement antenna are shown in Figs. 2(b) and (c). The antenna in Fig. 2(b) is tapered in the sense that the refractive index of the waveguide film varies along the direction of propagation, such that the refractive index difference between the waveguide film and cladding is gradually reduced near the output endface of the device. Hence, the confinement of the guided mode is reduced near this endface, resulting in an effective mode width D at the antenna output that is substantially larger than that of the nontapered waveguide. Therefore, the far-field beam divergence is also substantially reduced. For sufficiently thin waveguide films, reduced modal confinement can also be achieved by decreasing the waveguide film thickness, as shown in Fig. 2(c). In the experimental devices reported in this paper, reduced confinement of the guided mode is accomplished both by physically decreasing the waveguide dimension and by reducing the refractive index difference between the waveguide film and cladding along the length of the guide.

B. MBE Growth Technique

A GaAlAs slab waveguide with a monolithically integrated reduced-confinement antenna is shown schematically in Fig. 3. This antenna, which employs a compositionally and dimensionally tapered waveguide film, is produced by using a one-step MBE growth technique. The details of the MBE technique are as follows. The GaAs substrate wafer is bonded with indium to a specially designed substrate-mounting block whose top surface is slightly recessed in various regions.

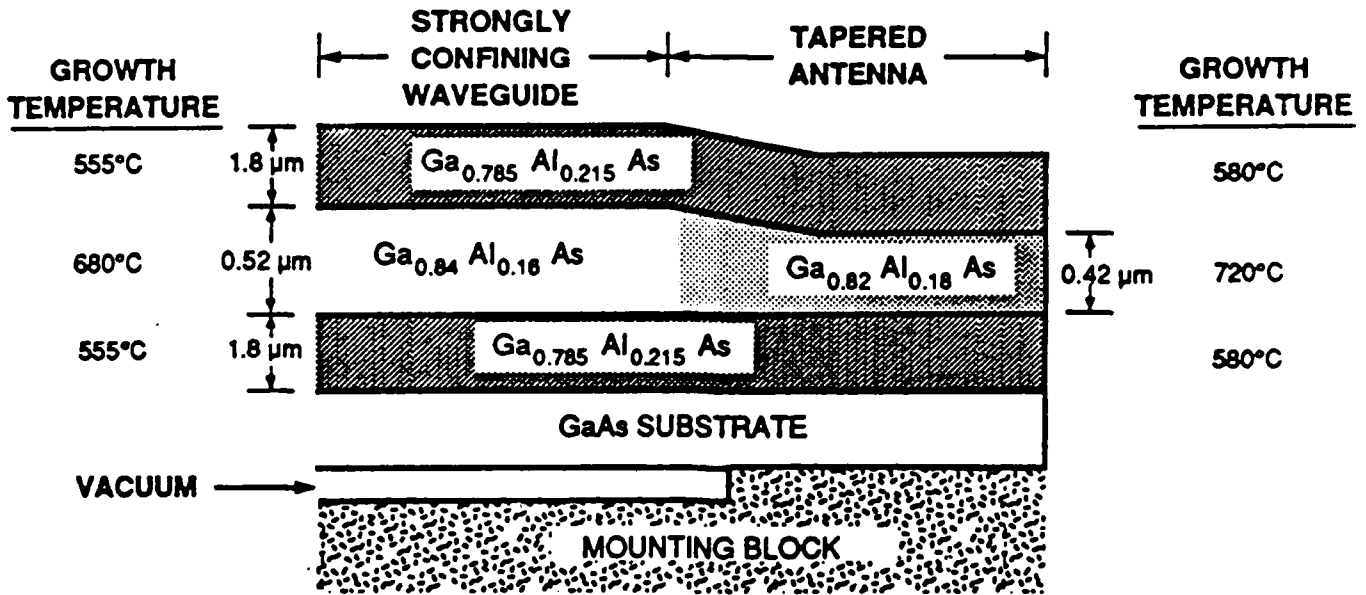


Fig. 3 Cross-sectional profile of a reduced-confinement GaAlAs tapered slab waveguide antenna. The material compositions and film thicknesses were obtained by Auger electron spectroscopy and photoluminescence measurements.

Figure 4(a) is an illustration of this molybdenum mounting block, and Fig. 4(b) is a cross-sectional profile of a portion of the mounting block and multiple-antenna wafer prior to cleaving. The regions of the wafer that are in direct thermal contact with the unrecessed portions of the mounting block are conductively heated, while the regions that are located above a recess are radiatively heated. The radiatively heated regions have a lower substrate surface temperature than the conductively heated regions of the same wafer. For substrate surface temperatures below 650°C, the sticking coefficients of both Ga and Al on GaAs are essentially independent of temperature. Above 650°C, however, the sticking coefficient of Ga continuously decreases with increasing temperature.^{8,9} This decrease in the Ga sticking coefficient results in increased Al concentrations and decreased growth rates for GaAlAs films grown by MBE at successively higher temperatures. Thus, for substrate surface temperatures greater than 650°C, a temperature gradient across the wafer surface produces a spatial variation in the relative amounts of Ga and Al that are incorporated into the waveguide film, as well as a spatial variation in the waveguide film thickness.

For the device shown in Fig. 3, a uniform 1.8- μm -thick $\text{Ga}_{0.785}\text{Al}_{0.215}\text{As}$ lower cladding layer is first grown at temperatures between ~555 and 580 °C, for which the sticking coefficients are insensitive to growth-temperature variations. The temperature of the mounting block is then increased and a tapered GaAlAs waveguide film is grown. For the film shown in Fig. 3, the substrate surface temperature ranges from ~680 to 720 °C. The resulting waveguide film varies from a 0.5- μm -thick $\text{Ga}_{0.84}\text{Al}_{0.16}\text{As}$ film in the cooler region to a 0.42- μm -thick $\text{Ga}_{0.82}\text{Al}_{0.18}\text{As}$ film in the warmer region. Finally, the mounting block temperature is reduced to ~580 °C and an upper cladding layer, identical in composition and thickness to the lower cladding layer, is grown. The layer thicknesses and compositions that are indicated in Fig. 3 were determined by Auger electron spectroscopy and photoluminescence measurements. With our current MBE growth procedure,

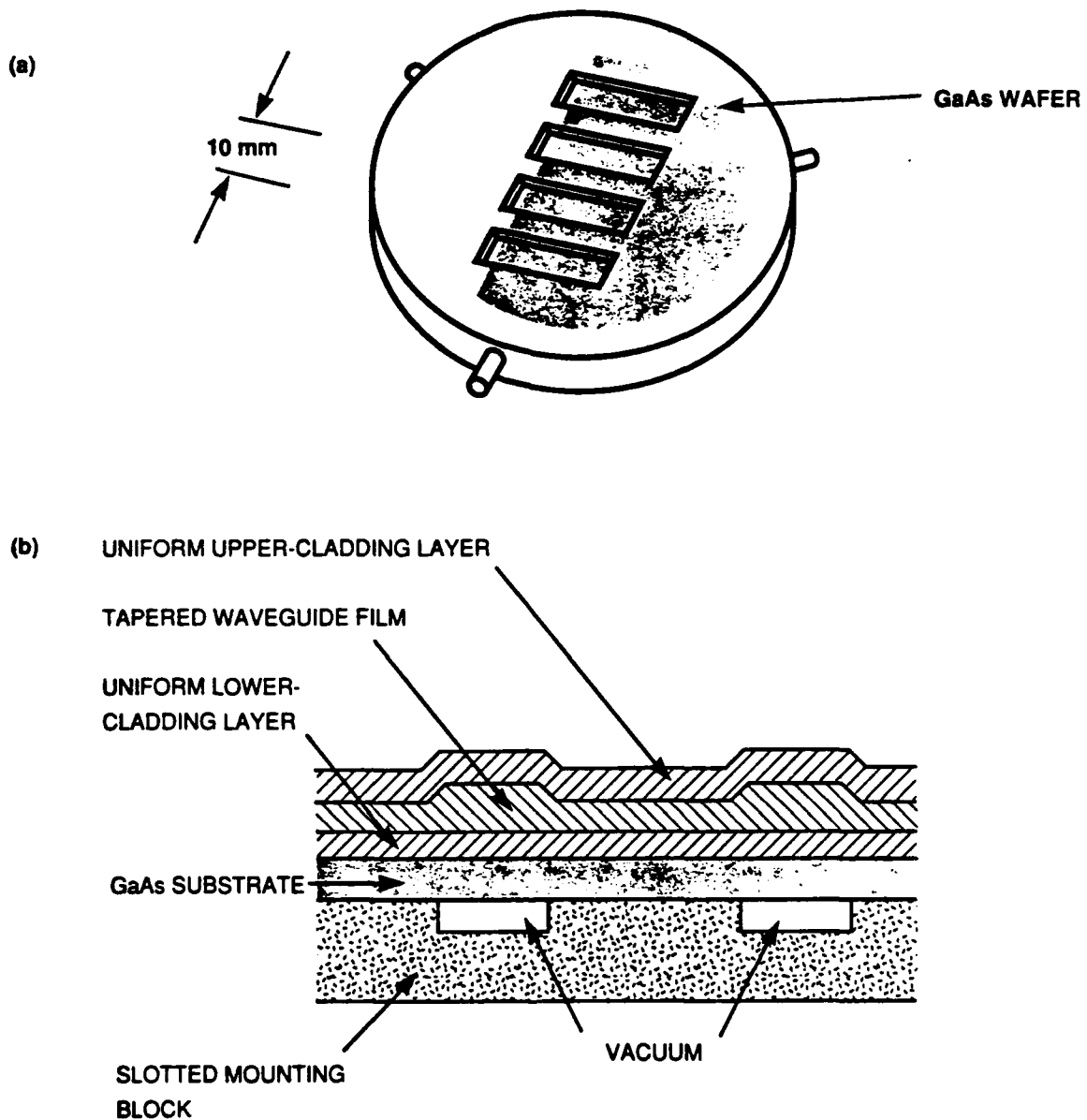


Fig. 4 (a) Slotted mounting block used during MBE growth to produce local variations in the substrate surface temperature.

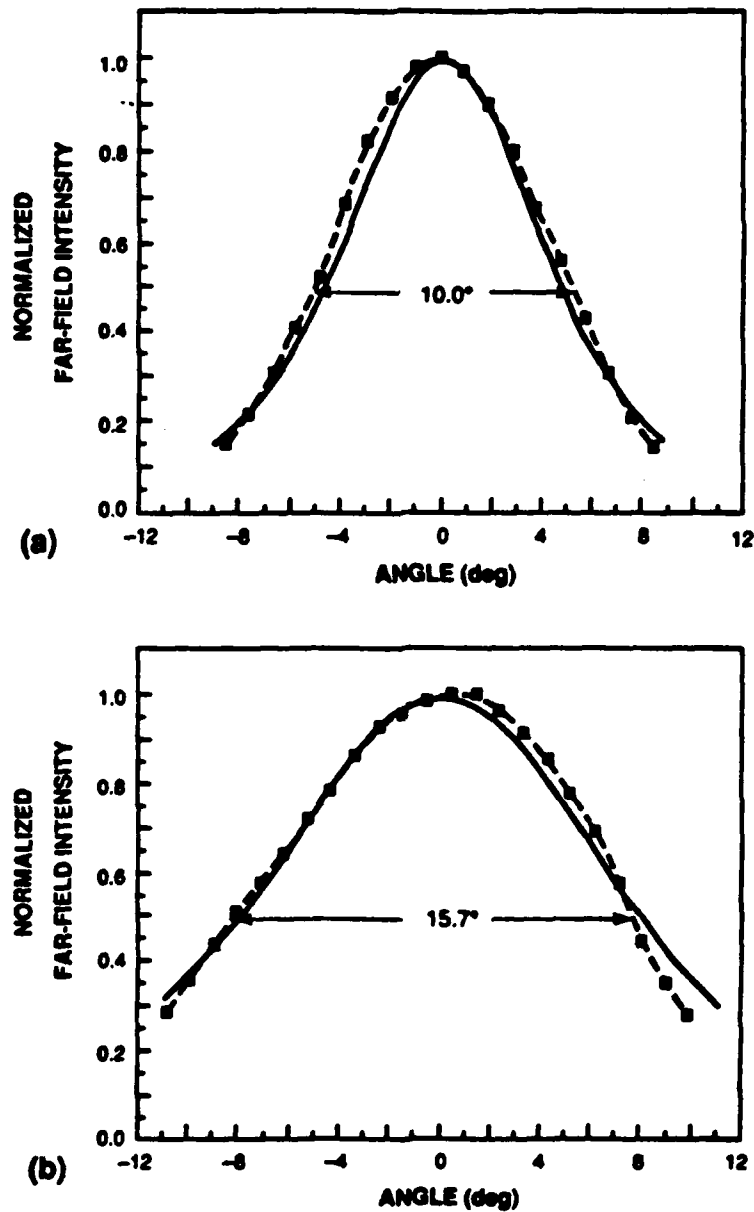
(b) Cross-sectional profile of a portion of the mounting block and multiple-antenna wafer prior to cleaving.

the length of the tapered transition is between 1 and 2 mm. By modifying this procedure, the taper length and geometry may be altered. Specifically, the depth and spacing of the mounting block recesses can be varied in order to controllably alter the taper profile. In addition, above 650°C, the Ga sticking coefficient is not strictly a linearly decreasing function of temperature. Therefore a variety of taper geometries can be produced by changing the temperature over which the graded index film is grown and adjusting the Al and Ga beam fluxes accordingly. Shorter taper lengths and customized taper profiles could also be achieved by using more sophisticated techniques such as laser heating to produce the substrate temperature gradients.

C. Experimental Results

The tapered slab waveguide antenna shown in Fig. 3 is designed for single-mode operation at a wavelength of 0.88 μm . In the cooler growth region, there is a difference of 0.055 in the AlAs mole fraction ($\Delta n = 0.022$) between the 0.52- μm -thick waveguide film and the cladding layers. The result is a strongly confining single-mode optical waveguide in this region, for which the confinement parameter $V = kh(n_f^2 - n_c^2)^{1/2} = 1.45$, where k is the magnitude of the wave vector, h is the film thickness, and n_f and n_c are the refractive indices of the film and cladding, respectively. The region grown at higher substrate surface temperatures, however, exhibits a difference of only 0.035 in AlAs mole fraction ($\Delta n = 0.014$), and the waveguide film thickness is only 0.42 μm . Hence, this section of the waveguide is much less optically confining ($V = 0.93$).

The data points and dashed line in Fig. 5(a) show the far-field intensity profile measured for the antenna of Fig. 3 along the direction perpendicular to the wafer surface. For comparison, the measured far-field profile for a nontapered device that maintains the strongly confining 0.52- μm -thick $\text{Ga}_{0.84}\text{Al}_{0.16}\text{As}$ waveguide film along its entire length is shown in Fig. 5(b). Both measurements are for transverse-electric (TE) polarized light from a GaAs diode laser at a wavelength



154272-1

Fig. 5 Normalized far-field intensity profiles for (a) tapered (reduced-confinement) and (b) nontapered GaAlAs slab waveguides. The data points and dashed lines indicate the experimentally measured profiles, while the solid lines indicate the theoretically predicted profiles based upon the Auger data. The experimental FWHMs are shown.

of $0.88\text{ }\mu\text{m}$. Radiation from the tapered-antenna waveguide exhibits a 10.0° full width at half-maximum (FWHM) far-field beam divergence, a 36% reduction from the 15.7° FWHM beam divergence obtained for the nontapered waveguide.

Using Auger data for both the strongly confining and weakly confining regions of the waveguide in Fig. 3, we have calculated the guided-mode parameters and the guided-mode electric-field amplitude profiles for the input and output sections of the device. According to these calculations, the width of the guided-mode intensity varies from $0.71\text{ }\mu\text{m}$ FWHM in the strongly confining waveguide region to $0.97\text{ }\mu\text{m}$ FWHM in the weakly confining structure, an increase of 37%. The analytically determined electric-field profiles for both regions of the device are then propagated to the far field through a Fourier transform. The theoretically predicted far-field intensity profiles, which are shown by the solid lines in Fig. 5, are in close agreement with the experimentally observed profiles for the tapered and nontapered waveguides.

Table I contains theoretical calculations of the mode size and far-field beam divergence for a nontapered GaAlAs slab waveguide, for an antenna with only a refractive index taper, and for an antenna with a combination of both refractive-index and dimensional tapers. The nontapered waveguide in Table I has the same waveguide parameters as the strongly confining input region of the device in Fig. 3, and the antenna with both the refractive index and dimensional tapers corresponds exactly to the antenna illustrated in Fig. 3. The FWHMs correspond to the theoretical curves of Fig. 5. For completeness, Table I includes the calculated mode parameters and beam divergence for a device incorporating only a refractive index taper, which is the structure that would exist if only a refractive index taper, and no dimensional taper, were present in the device of Fig. 3. For such a structure, the calculated width of the guided-mode intensity at the output is $0.91\text{ }\mu\text{m}$ FWHM and the calculated far-field beam divergence is 11.0° FWHM. Hence, for the antenna illustrated in Fig. 3 and for the results reported in Fig. 5, the

Table I
Relative Effects of the Refractive Index and Dimensional Tapers

	Waveguide Film Thickness (μm)	AlAs Mole Fraction in Waveguide Film	AlAs Mole Fraction in Cladding	Theoretical Mode Width at Antenna Output (FWHM μm)	Theoretical Far-Field Beam Divergence (FWHM deg)
Nontapered waveguide	0.52	0.16	0.215	0.71	15.9
Tapered antenna (refractive index taper only)	0.52	0.16 \rightarrow 0.18	0.215	0.91	11.0
Tapered antenna (refractive index and dimensional taper)	0.52 \rightarrow 0.42	0.16 \rightarrow 0.18	0.215	0.97	9.4

refractive index taper accounts for ~75% of the reduction in the transverse far-field beam divergence, while the dimensional taper accounts for the remaining ~25% of the reduction. Therefore, for this particular device, the refractive index taper is the predominant effect responsible for the increase in the far-field beam directionality; however, the combination of refractive index and dimensional tapering produces a net reduction in the far-field beam divergence that is greater than that of either of these effects acting alone.

To examine the limits on the performance of reduced-confinement antennas, we have grown the tapered waveguide structure shown in Fig. 6(a). This device tapers from a symmetric slab waveguide in the cooler growth region to uniform material (no waveguide structure) in the warmer growth region. The structure has been cleaved into a series of samples whose output endfaces intersect the waveguide antenna at various positions along the taper length, as indicated by the dashed vertical lines in Fig. 6(a). The measured far-field profiles for these devices are

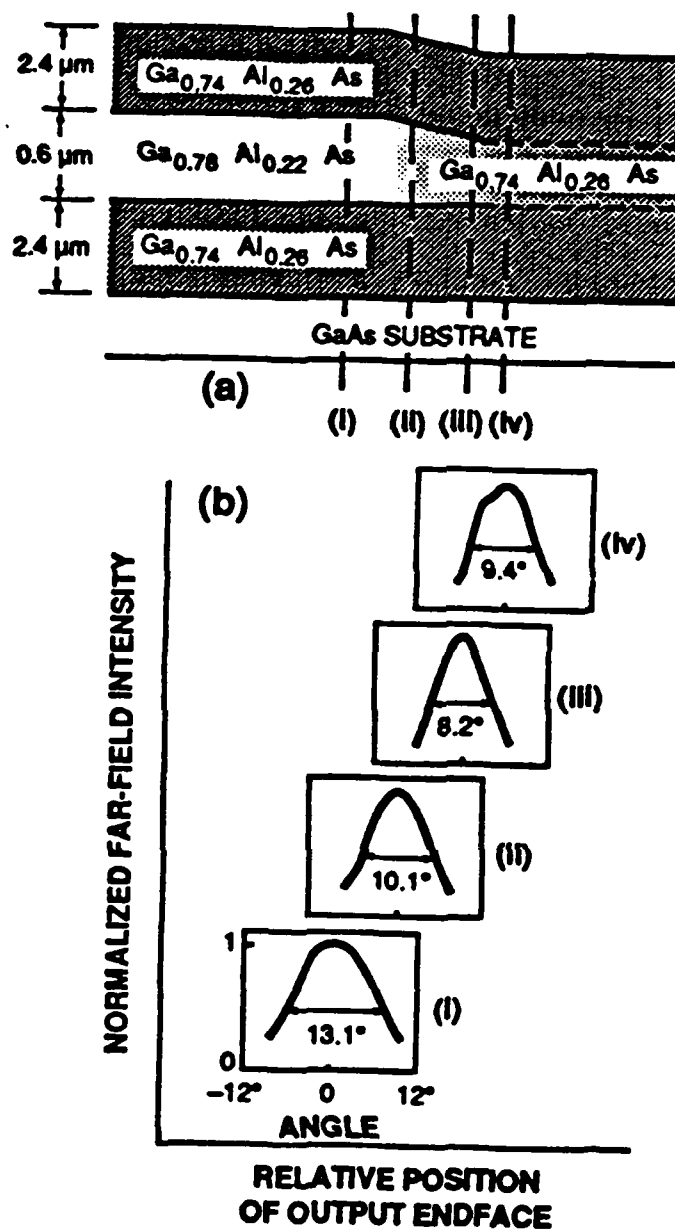


Fig. 6 (a) Cross-sectional profile of a reduced-confinement structure that tapers from a buried symmetric slab waveguide to uniform material. The dashed vertical lines indicate the locations of the cleaved output endfaces of samples (i) through (iv). (b) Experimentally measured far-field profiles for samples (i) through (iv).

shown in Fig. 6(b). The nontapered device (i), with its uniform 0.60- μm -thick $\text{Ga}_{0.78}\text{Al}_{0.22}\text{As}$ waveguide film, exhibits a 13.1° FWHM far-field beam divergence. As the location of the antenna endface progresses through the tapered transition, the divergence steadily decreases, eventually reaching a minimum value at (iii) of 8.2° FWHM. This 8.2° divergence is a 37% reduction from the divergence for the nontapered waveguide. The output endface of the longest sample (iv) lies beyond the tapered transition, in the region of the wafer where the structure is no longer guiding. As expected, significant leakage into the higher-index GaAs substrate is apparent in the far-field profile for this device, causing an increase in the divergence to 9.4° FWHM.

The minimum beam divergence of 8.2° FWHM in Fig. 6(b) can be interpreted as follows. As the GaAs-laser radiation propagates through the tapered transition, the waveguide structure becomes significantly less confining and the width of the guided mode increases until it approaches 5.4 μm , the total thickness of the transparent guiding and cladding layers. The lower boundary of this transparent epitaxial window is the absorbing higher-index GaAs substrate. As a benchmark for comparison with our experimental measurements, we have calculated the theoretical far-field radiation profile for a 5.4- μm -wide slit that is uniformly illuminated by a plane wave. The central far-field lobe of this calculated $[(\sin x)/x]^2$ intensity pattern is 8.2° FWHM. Although the "exact" agreement is fortuitous, this result indicates that the observed 8.2° FWHM far-field beam divergence is consistent with the minimum beam divergence that can be expected for this particular device. In order to obtain a 5° FWHM transverse far-field beam divergence, we have calculated that an emitting aperture thickness greater than 9 μm is required. Fabrication of tapered waveguide structures that incorporate thicker cladding layers than those shown in Fig. 6(a) is currently under way in an effort to demonstrate far-field beams with significantly less divergence. N^+ -GaAs doped substrates are

being used for these devices to absorb light radiating outside of the cladding and into the substrate.

To date, quantitative loss measurements have not been performed on channel or ridge waveguides fabricated in the reduced-confinement GaAlAs tapered waveguide material. Current research efforts are focussed on performing these loss measurements. The technique that has been developed to measure this loss uses the fact that a waveguide structure cleaved at both ends behaves as a Fabry-Perot resonator. Measuring the transmission ratio of this resonator one can determine the loss in the waveguide.¹⁰ For this measurement a laser source is required with a long coherence length (a single spectral mode with very narrow linewidth). Gas lasers have been used by others for this purpose.¹⁰ However, the antennas being developed are for use at GaAs diode laser wavelengths. An appropriate laser source has been developed by stabilizing the operating temperature of a GaAs diode laser which had been manufactured for coherent communication. By observing the transmission ratio of the power as the cleaved waveguide device changes length due to slow heating, the optical attenuation can be calculated. Losses as low as 0.7 dB/cm have been measured on channel waveguides made in material grown by the OMCVD (Organo-Metallic Chemical Vapor Deposition) technique and whose fabrication is described in Section IV.

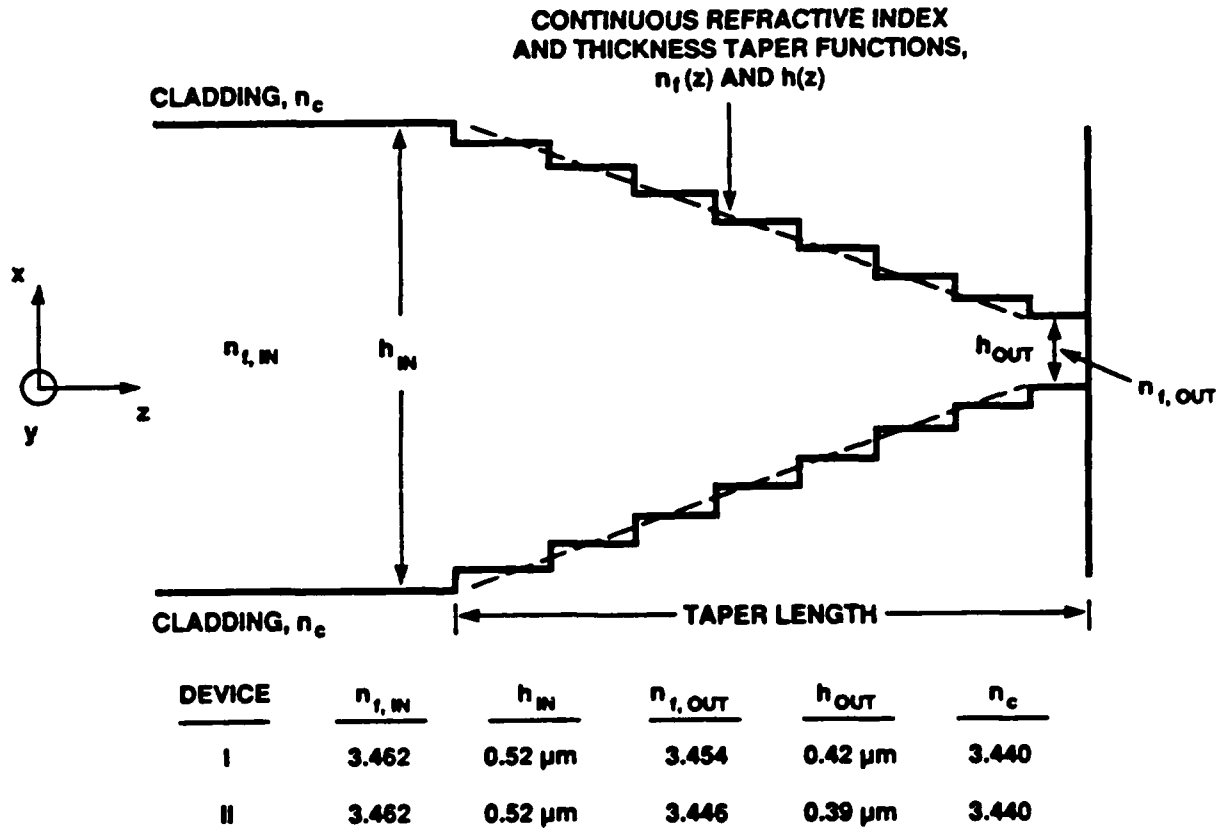
Straight and tapered channel waveguides are being fabricated from the antenna material grown using MBE. The straight channel waveguide devices are necessary to quantify the optical loss due to the material alone. This channel waveguide will then be integrated with the tapered film device to identify the loss due to the antenna region. In addition to straight waveguides, tapered channel waveguides will be fabricated using an Ion Beam Assisted Etching (IBAE) process. A mask set for the photolithography has already been designed for a tapered channel waveguide. This taper is etched in the lateral direction and provides the second dimension of tapering in addition to the transverse tapering already

occurring in the film layer. This tapered waveguide will be fabricated using the MBE grown material without and with the film taper. A comparison of these two devices will allow one to determine where any power losses may occur due to the channel taper. The final device will provide a two-dimensional reduced-confinement antenna since the film taper will be integrated with the channel taper.

D. Numerical Simulation

A numerical simulation routine has been developed in order to verify and accurately predict the performance limitations of reduced-confinement antennas. Fraunhofer diffraction theory dictates that the far-field beam divergence is a function of both the amplitude and phase profiles of the electric field at the antenna output. For very long tapers, the reduced-confinement antenna is adiabatic, meaning that the optical power remains in the local guided mode and the optical field maintains a planar phase front. For shorter tapers, however, this is not always the case. Through the use of numerical simulation, we have found that requirements on both the amplitude and phase profiles of the electric field at the antenna output impose a stringent lower limit on the acceptable taper length for optimal far-field antenna performance. In addition, this lower limit on acceptable taper length is found to be a function of both taper geometry and the relative degree of variation in the confinement of the guided mode along the antenna.

For the numerical simulation, the continuously tapered reduced-confinement slab waveguide antenna is modeled by a step-tapered slab waveguide section of the type illustrated in Fig. 7. Both the refractive index and thickness of the waveguide film are chosen to vary along the direction of propagation with an assumed taper function. For the first set of results that are described in this paper, the waveguide refractive index and film thickness are assumed to vary linearly from the input index and thickness given by $n_{f,in}$ and h_{in} , respectively, to the output index



150450-5

Fig. 7 Symmetric step-tapered slab waveguide model of a continuously tapered reduced-confinement antenna, assuming linearly tapered refractive index and thickness profiles. Dashed lines represent the continuous refractive index and thickness taper functions, while the solid lines represent the step-tapered waveguide functions that are analyzed. The output endface of the antenna coincides with the very end of the tapered transition. The input and output waveguide parameters are listed for two simulated antennas. (Device I corresponds to the experimental structure illustrated in Fig. 2.)

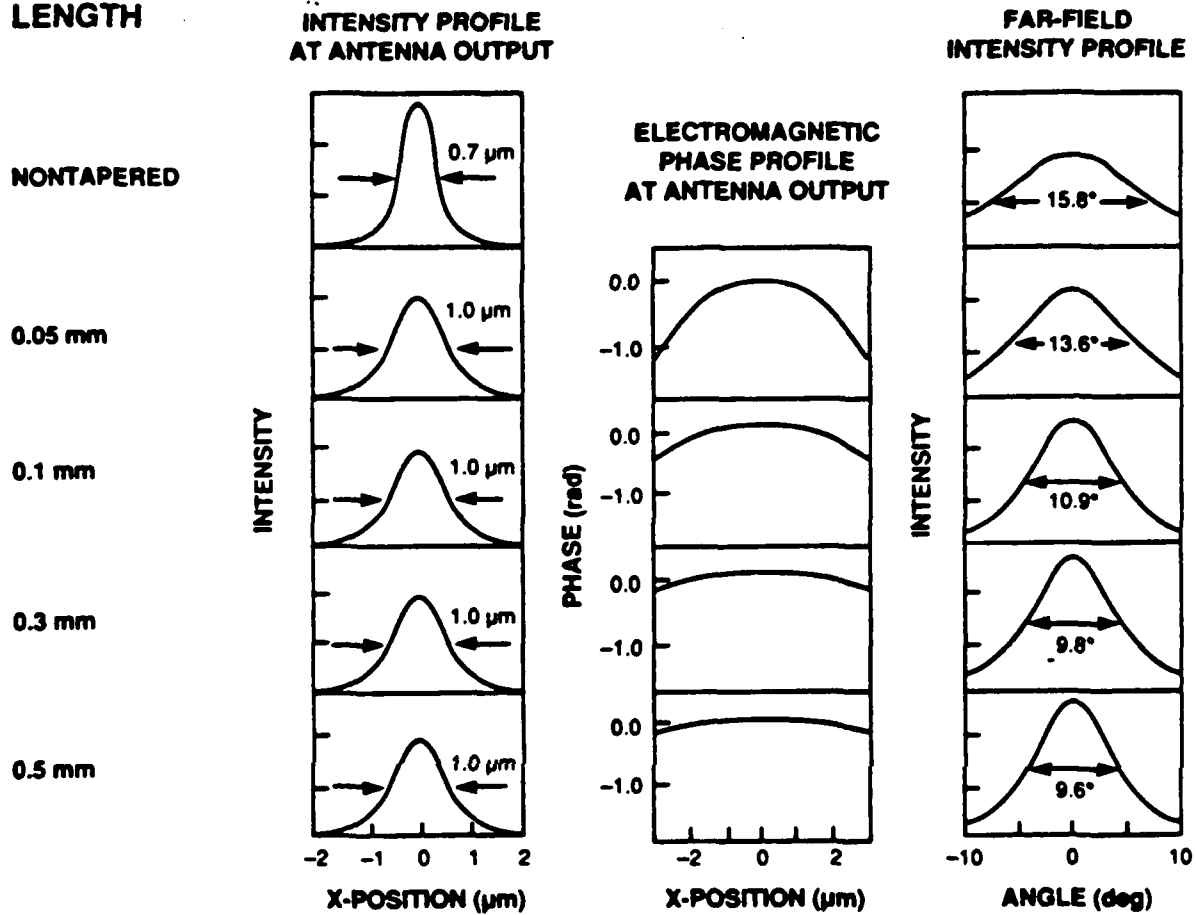
and thickness given by $n_{f,out}$ and h_{out} , respectively. The output endface of the waveguide antenna is assumed to coincide with the very end of the tapered transition.

By breaking the tapered antenna into a large number of short discrete steps (50 to 100) and by utilizing the concept of local normal modes, a procedure very similar to that described by Suchoski and Ramaswamy¹¹ is used to analyze the effects of the tapered transition on the optical beam. Specifically, the local fundamental guided mode and the spectrum of local radiation modes are determined in each of the waveguide sections. By applying the boundary conditions for Maxwell's equations at each step discontinuity, and by allowing the local guided and radiation modes of each waveguide section to propagate with the appropriate propagation constants, the amplitude and phase profiles of the total electric field are calculated as an optical beam passes through the tapered antenna structure.

This report describes the simulated performance of two GaAlAs slab waveguide antennas, devices I and II, whose input and output waveguide parameters are listed in the table at the bottom of Fig. 7. Device I has input and output waveguide parameters that correspond exactly to the input and output parameters for the experimental antenna illustrated in Fig. 3. Device II has the same input parameters as device I. However, the output of device II is somewhat less confining than that of device I, indicating that the waveguide film index is closer to that of the substrate and the film is slightly thinner. Hence, a greater reduction in the far-field beam divergence is anticipated from device II than from device I.

The effects of taper length on antenna performance are illustrated in Fig. 8 for the case of device I, assuming a linearly tapered antenna. Specifically, Fig. 8 shows as a function of taper length the simulated intensity and phase profiles of the electric field at the output of device I, as well as the simulated far-field intensity profiles. The near-field and far-field intensity profiles for a nontapered device with a 0.52- μ m-thick strongly confining waveguide film

**TAPER
LENGTH**



190480-4

Fig. 8 Effects of taper length on antenna performance for device I, assuming linearly tapered index and thickness profiles. The intensity and phase profiles of the electric field at the antenna output and the far-field intensity profiles are shown for various taper lengths.

($n_f = 3.462$) along its entire length are included, for comparison, in Fig. 8. For this nontapered waveguide, the width of the guided-mode intensity profile measures $0.7 \mu\text{m}$ FWHM, resulting in a 15.8° FWHM far-field beam divergence. For taper lengths as short as $50 \mu\text{m}$, the width of the output optical beam from device I is increased by $\sim 50\%$ to $1.0 \mu\text{m}$, when compared to the nontapered waveguide, as a result of the reduced-confinement antenna. However, for taper lengths less than $300 \mu\text{m}$ this increase in the width of the output optical beam is accompanied by a diverging phase front curvature across the electric field at the antenna output, as shown in Fig. 8. When the far-field radiation profile is calculated using both the amplitude and phase profiles of the electric field at the output, suboptimal antenna performance is achieved in the case of these extremely short tapers as a result of the induced phase-front curvature. In terms of our local-normal-mode analysis, this phase-front curvature for short devices results from a small fraction of the optical field that has coupled into radiation modes; because of an insufficient phase delay, this radiation does not couple efficiently back into the guided mode. Although the total power contained within the local radiation modes at the antenna output is small (only a few percent of the total power), the radiation modes are able to significantly alter the phase of the electric field in the tails of the optical beam. In the case of device I, on the assumption of linearly tapered refractive index and thickness profiles, near optimal antenna performance is only achieved for taper lengths greater than $300 \mu\text{m}$.

Figure 9(a) shows as a function of taper length the fraction of the input optical power that is contained within the local radiation modes at the antenna output of devices I and II. Note that a logarithmic scale is used and a linear taper profile is assumed. Figure 9(b) shows the FWHM far-field beam divergence also as a function of taper length for both of these linearly tapered devices. For device I, which corresponds to the experimental antenna in Fig. 3, nearly optimal

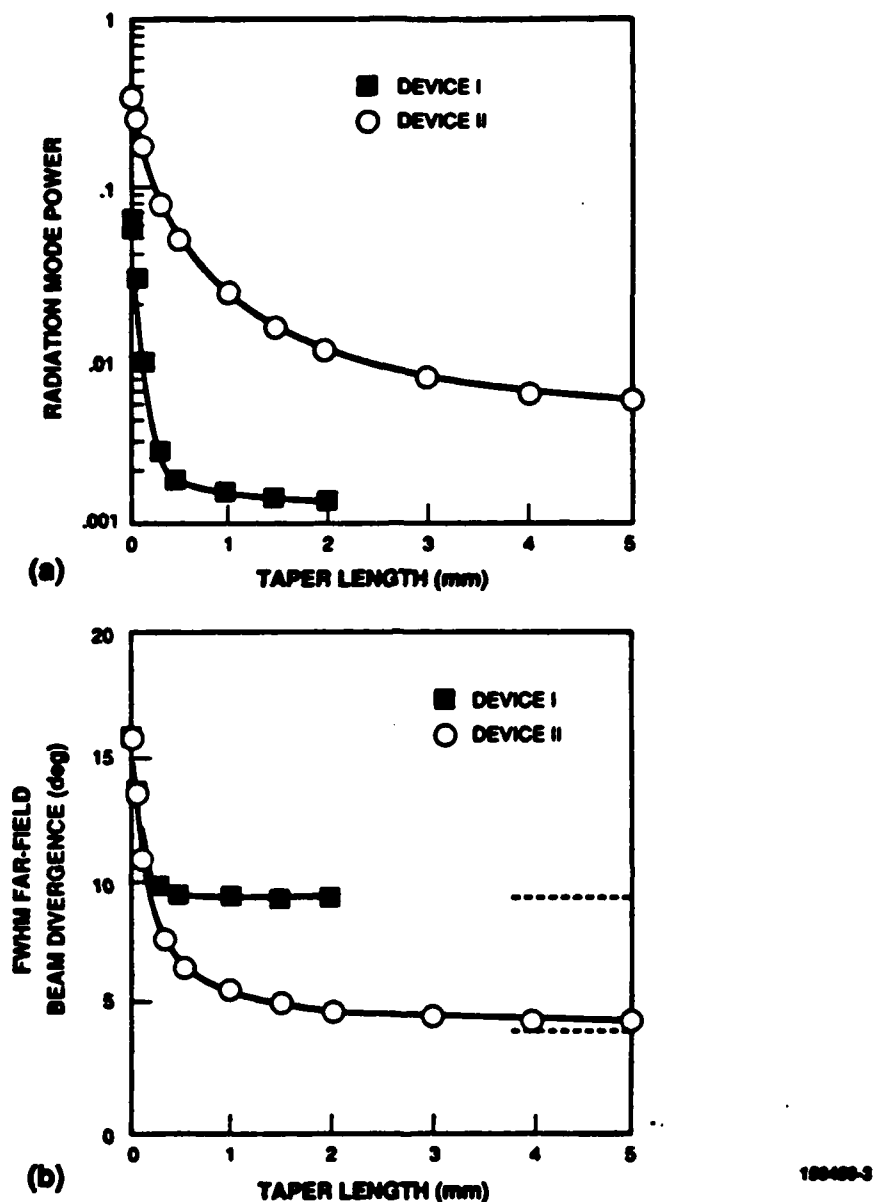


Fig. 9 (a) Fraction of input power that does not couple into the local guided mode at the antenna output as a function of taper (antenna) length. A logarithmic scale is used to accentuate the differences between devices I and II. (b) FWHM far-field beam divergence for devices I and II as a function of taper length. The horizontal dashed lines indicate the minimum anticipated far-field beam divergence for the two devices, based upon the loosely confined local guided mode at the antenna output. These curves assume linearly tapered refractive index and thickness profiles.

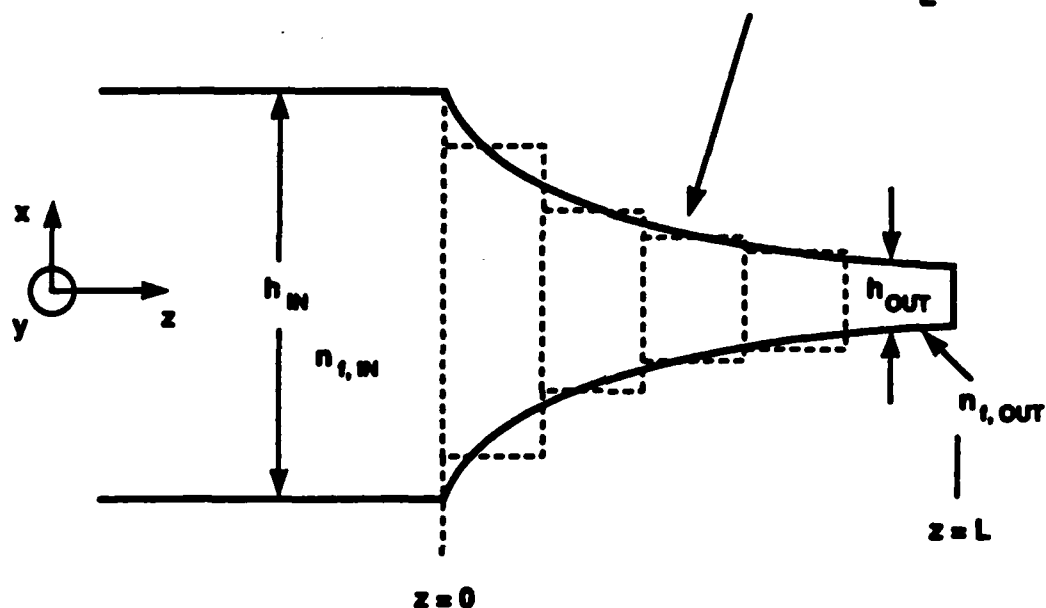
antenna performance is achieved for taper lengths greater than 300 μm , resulting in a ~40% reduction in the transverse far-field beam divergence. For device II, which achieves a lower degree of beam confinement at the antenna output, a ~70% reduction is achieved; however, the necessary taper length for optimal antenna performance is increased to ~2 to 3 mm.

The effects of taper geometry on antenna performance have also been investigated. In addition to the linearly tapered profile illustrated in Fig. 7, a parabolically tapered antenna has been examined, in which the refractive index and thickness of the waveguide film vary parabolically along the direction of propagation as shown in Fig. 10.¹² Compared with the linear antenna, the parabolically tapered geometry results in a more steady increase in the size of the optical mode as the beam propagates along the tapered transition. A comparison of the performance of device II for the linear- and parabolic-taper cases is shown in Fig. 11. As expected, nearly optimal antenna performance can be achieved with a shorter taper length by using a parabolic antenna in place of the linear antenna. Specifically, for the parabolically tapered structure, a 70% reduction in the far-field beam divergence, from 16° to 5° FWHM, is attainable from a 1-mm-long antenna for which the cladding and film thicknesses total >9 μm . In addition, the simulation indicates that a negligible fraction (<1%) of the input optical power is lost to radiation modes as a result of this 1-mm-long parabolically tapered antenna.

PARABOLIC TAPER PROFILES

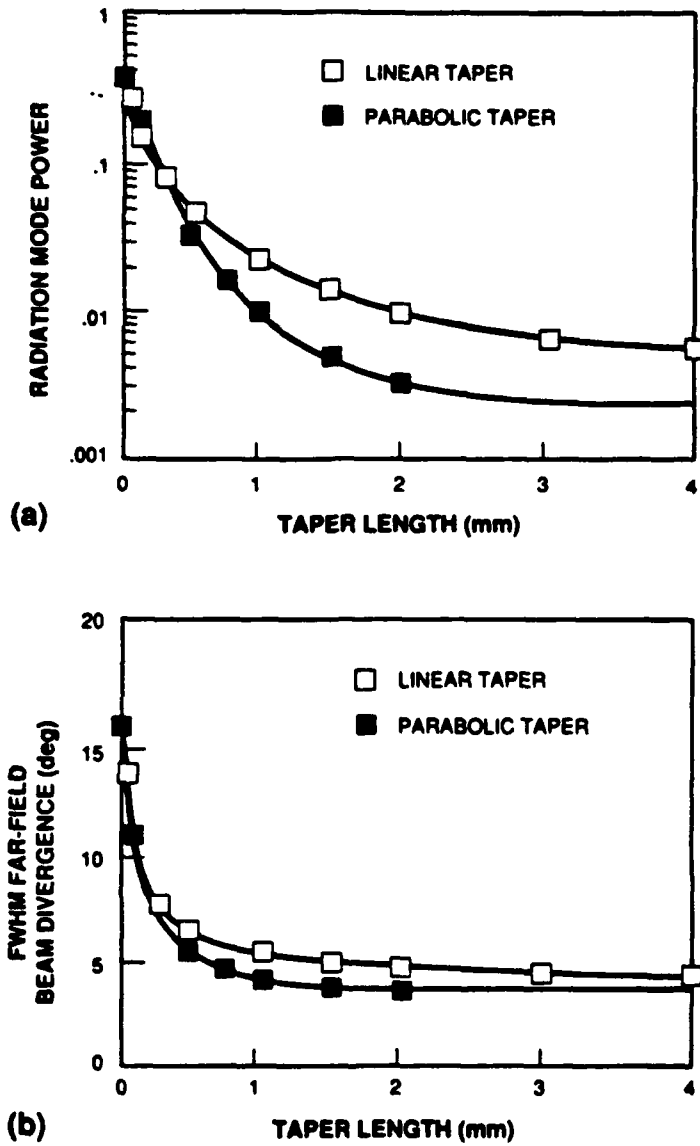
$$n_t(z) = n_{t,OUT} + (n_{t,IN} - n_{t,OUT}) \cdot \frac{(z-L)^2}{L^2}$$

$$h(z) = h_{OUT} + (h_{IN} - h_{OUT}) \cdot \frac{(z-L)^2}{L^2}$$



151725-2

Fig. 10 Schematic of a reduced-confinement antenna with parabolically tapered refractive index and thickness profiles. The solid lines represent the continuous refractive index and thickness taper functions, while the dashed lines represent the step-tapered waveguide functions that are analyzed. The output endface of the antenna coincides with the very end of the tapered region.



180480-1

Fig. 11 Comparison of the performance of device II for linearly and parabolically tapered antennas. (a) Fraction of input power that does not couple into the local guided mode at the antenna output as a function of taper (antenna) length. (b) FWHM far-field beam divergence as a function of taper length.

IV. Wavefront Phase Tilt Measurement

In the wavefront sensing and correction basic module, the input powers to the interferometer arms will not be equal, as a result of input power nonuniformity or unequal coupling by the evanescent couplers. The requirement that the coupling of the evanescent couplers be equal for a system with a large number of modules ($10^3 - 10^4$) is unrealistic. In integrated optics, as in integrated circuits, it is important to relax the requirements on individual components and require that the operation of the integrated optics (circuits) be independent of significant component variations. Therefore, two optical wavefront phase tilt measurement configurations have been developed theoretically to measure the wavefront phase tilt, regardless of power non-uniformity. The first consists of a Y-junction interferometer with a phase dither applied to one of the input arms. The second consists of a three-guide coupler with inputs to the outer arms; a square-wave bias phase function, which switches between zero and $\pi/2$ radians, is applied to one of the input arms.

The output power of a Y-junction interferometer with equal powers in the input arms is given by Equation 1 in Section II. For unequal powers and unequal evanescent coupling from the straight-through waveguides to the interferometer arms, the output power of the Y-junction is given by,

$$P_{\text{out}} = [\delta_1 P_1 + \delta_2 P_2 + 2/\delta_1 P_1 / \delta_2 P_2 \cos\phi] B \quad (2)$$

where P_1 and P_2 are the unequal incident powers, δ_1 and δ_2 are the unequal coupling coefficients of the evanescent couplers, B again accounts for additional losses in the interferometer arms, and ϕ is the phase difference between the arms.

Extracting the phase difference ϕ from this equation requires measuring the powers in the output arms, the coupling from each evanescent coupler, and the loss in the arms of the interferometer.

We have designed two wavefront phase tilt measurement techniques to measure the phase difference ϕ without tapping the power in the interferometer arms or measuring the coupling coefficients of the sampling couplers. The first technique shown in Fig. 12 consists of a Mach-Zehnder interferometer with a sinusoidal phase dither applied to one of the interferometer arms. The output of the Y-junction is given by

$$P_{out} = E_1^2 + E^2 + 2E_1E \cos (\phi - \Gamma \sin \omega t) \quad (3)$$

where E_1 and E_3 are the electric fields in the arms of the interferometer and are related to the unequal input powers, P_1 and P_3 , the coupling coefficients of the samplers, δ_1 and δ_3 , and the loss in the interferometer arms, B ; and $\Gamma \sin \omega t$ is the phase dither in the interferometer arm. For a small amplitude phase dither, the phase tilt ϕ can be determined from the ratio of the amplitudes of the first and second harmonic terms, which eliminates any dependence on the unequal electric fields, powers and coupling coefficients in the system, as well as the loss in the interferometer arms.

The second wavefront phase tilt measurement technique that has been designed shown in Fig. 13, uses a three-guide coupler and a phase switching bias function, applied to one of the input arms. The applied phase bias switches between zero and $\pi/2$ radians. For a three-guide coupler which is one coupling length long, a coupled mode theory analysis can be used to derive the equations for the three output powers of the guides. By manipulating these output powers, and taking the appropriate ratio for the case of no phase shift to the case of $\pi/2$ phase shift, the phase difference between the input arms ϕ can again be determined. Once again the dependence on the unequal electric fields, coupling coefficients and loss in the input arms is eliminated.

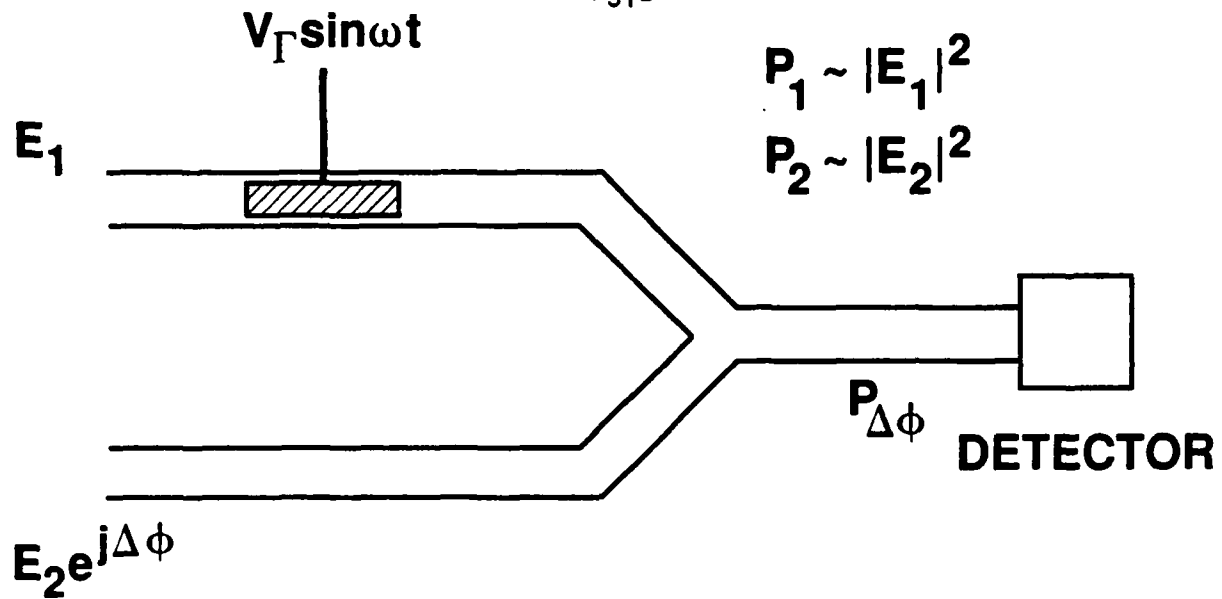


Fig. 12 The Y-junction interferometer and phase dither technique for measuring the phase difference.

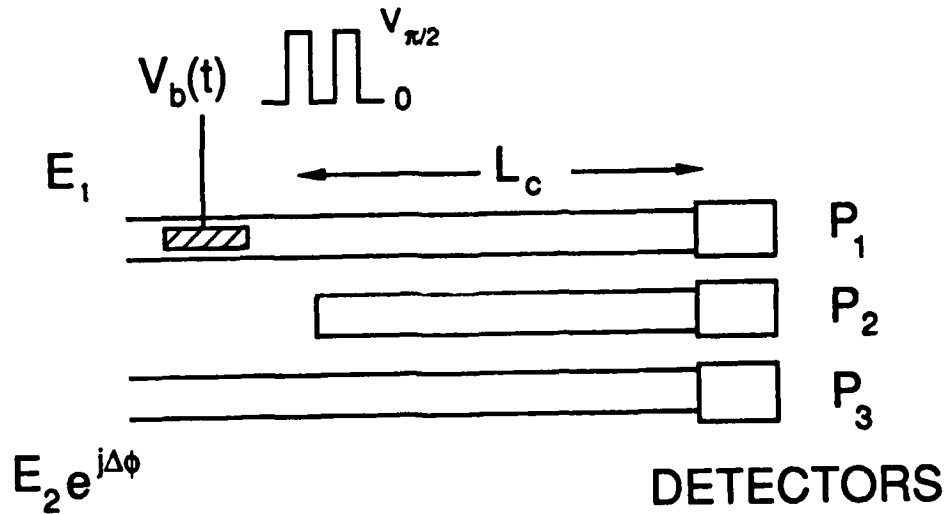


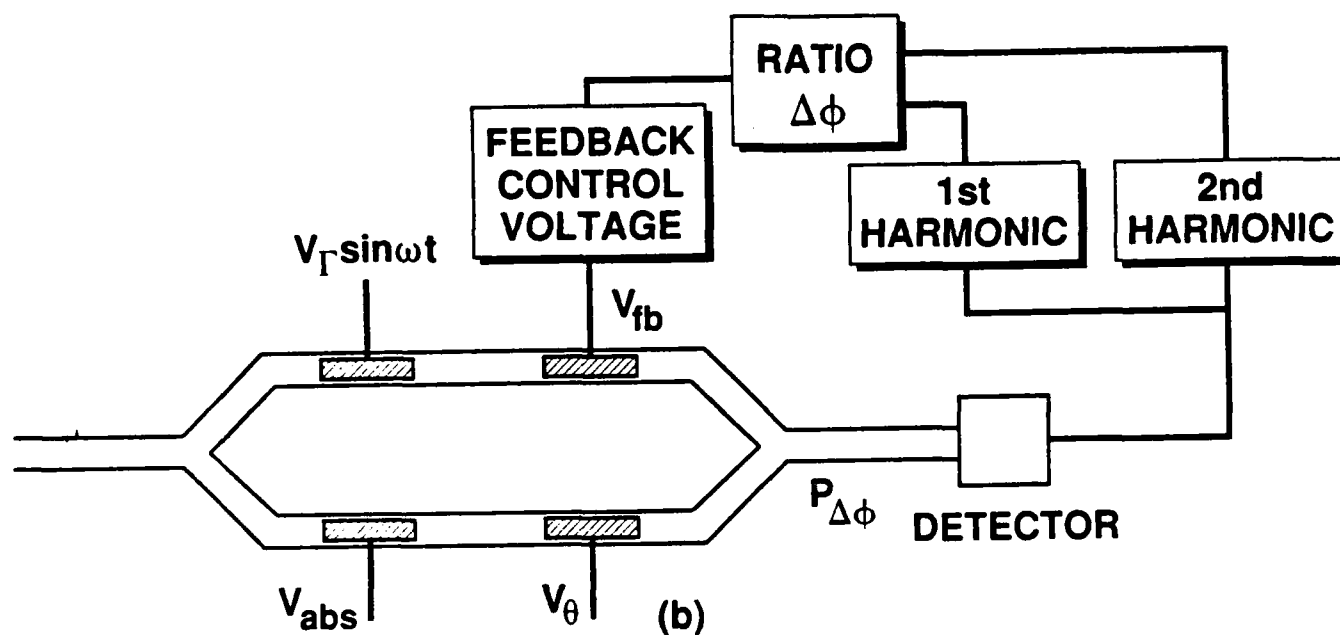
Fig. 13 The three-guide coupler and phase-switching technique for measuring the phase difference.

For the first design, which uses the Mach-Zehnder interferometer, an experimental system is being built to validate the design. In this proof-of-concept AlGaAs Mach-Zehnder system, illustrated in Fig. 14, there are four p-n junction phase modulators, two on each arm of the interferometer. The sinusoidal dither voltage is applied to one electrode, a voltage V_0 to vary the phase in one arm applied to a second electrode, and the feedback voltage used to maintain a zero phase difference between the output of the two arms applied to a third electrode. The fourth electrode can be forward biased to investigate amplitude as well as phase changes. In this test structure, output power is detected off-chip with a silicon detector and the amplitudes of the first and second harmonics of the detector output synchronously measured with lock-in amplifiers. A computer is used to calculate the phase difference, and apply an appropriate feedback voltage. The equipment used in the feedback loop is IEEE-488 compatible so that the computer can be used to control phase measurement and correction via the GPIB interface bus. Since the ultimate system will use on-chip circuitry, the optical components were designed compatible with GaAs electronic circuit technology.

For the sinusoidal phase dither applied to one arm of a Y-junction interferometer [Fig. 14], the output power is given by,

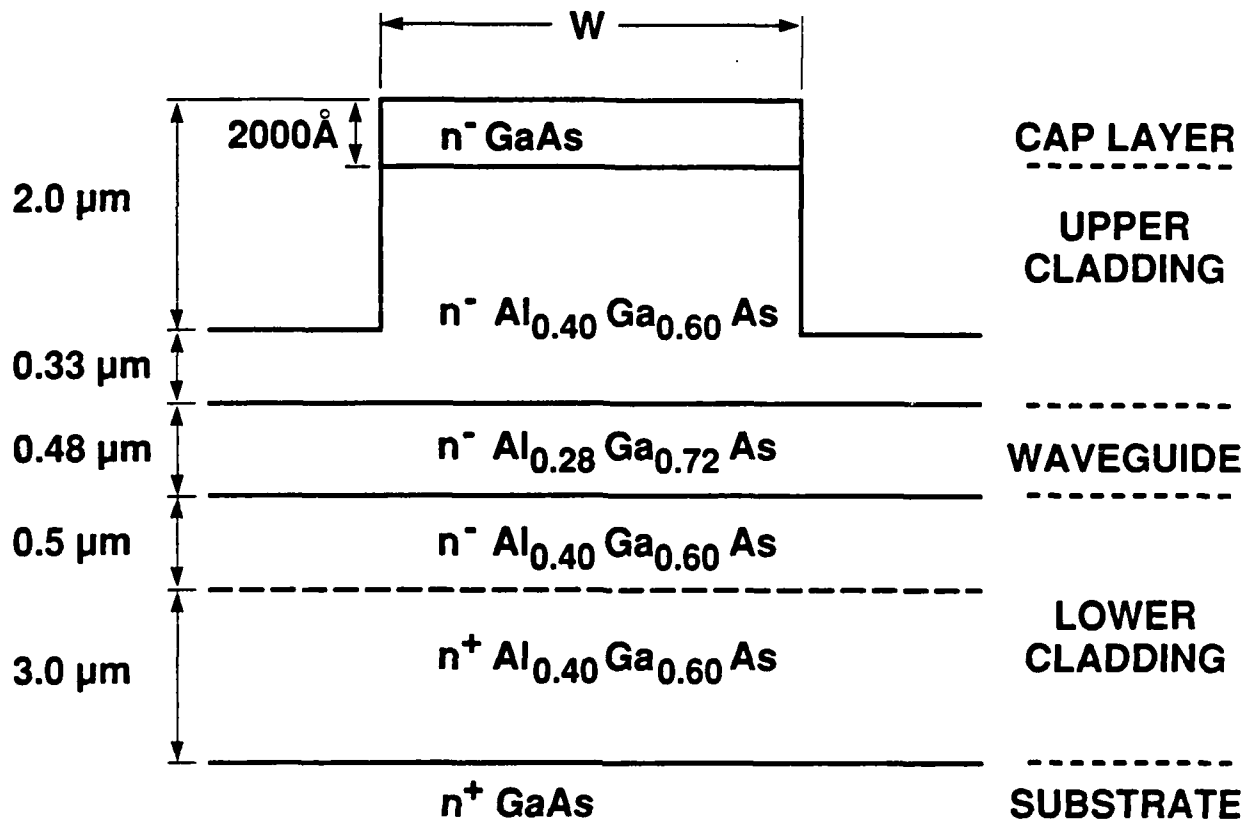
$$P_{\Delta\phi} = P_1 + P_2 + 2 \sqrt{P_1 P_2} \cos(\Delta\phi - \Gamma \sin\omega t) \quad (4)$$

where P_1 and P_2 are the powers in the interferometer arms incident on the second Y-junction and $\Gamma \sin\omega t$ is the phase dither. For known dither, the phase difference $\Delta\phi$ can be determined from the ratio of the amplitudes of the first and second harmonics of the dither frequency independent of the power variations. In addition to being insensitive to input power variations, this technique also allows for greater fabrication tolerances.



165904-1

Fig. 14 The proof-of-concept AlGaAs Mach-Zehnder experimental system used to validate the phase measurement and correction. The sinusoidal dither voltage is applied to the first electrode, a voltage V_θ to vary the phase in one arm applied to the second electrode, the feedback voltage V_{fb} applied to the third electrode, and a forward-biased voltage V_{abs} to investigate phase and amplitude changes applied to the fourth electrode.



165904-2

Fig. 15 Cross section of the dielectric-loaded strip heterostructure waveguides for use at GaAs laser wavelengths. The waveguides are single mode at $\lambda = 0.88 \text{ \mu m}$ for $W < 4.4 \text{ \mu m}$. For the phase modulators, part of the upper cladding was doped p^+ (with the p^+ - n junction located about 0.5 \mu m from the waveguide-cladding interface), and a AuZnAu top contact was used.

Dielectric-loaded strip heterostructure waveguides (Fig. 15) designed for operation at GaAs laser wavelengths were used in the interferometer. The epilayers were grown by organometallic vapor phase epitaxy (OMVPE), and ribs etched in the upper cladding layer of the waveguide structure by reactive ion etching (RIE) for two-dimensional optical confinement. This four-layer structure was modelled theoretically and single-mode waveguides designed to minimize absorption loss (low carrier concentration in the waveguide layer), scattering loss (the optical mode is away from the etched interfaces), and radiation loss in abrupt bends and Y-junctions (the optical mode is well-confined). Waveguides were characterized for propagation loss (<1 dB/cm) using the Fabry-Perot loss measurement technique described on page 19 in Section IIIC above. Measurements were also made of the angular dependence of abrupt bend insertion loss (0.20 dB/bend for 0.5° angle) and Y-junction insertion loss (0.37 dB for 1.0° full angle). Selective Be^+ ion implantation followed by rapid thermal annealing can be used to form the p^+-n-n^+ phase modulators. The measured characteristics of these phase modulators has been compared with theoretical results of both a perturbation analysis and a more exact analysis of the waveguide mode in the presence of an electric field.

The waveguide opto-evaluation testbed at the Research Laboratory of Electronics became operational during the second year of this contract. MIT completely renovated the laboratory and installed a sophisticated air conditioning system with accurate humidity control. The testbed has the appropriate optics, laser sources, detectors and camera systems for evaluating integrated optical waveguide structures at laser wavelengths of $0.875\text{ }\mu\text{m}$, $1.15\text{ }\mu\text{m}$ and $1.3\text{ }\mu\text{m}$. Loss measurements can be made using the Fabry-Perot measurement technique at $0.875\text{ }\mu\text{m}$ and $1.15\text{ }\mu\text{m}$. A scanning mirror in the output path can be used to scan the output mode profile of the waveguide devices (e.g. directional couplers and Y-junctions). The testbed is IEEE-488 compatible and is controlled with GPIB interface bus with a PS/2 Model 80 computer given to MIT under a grant from IBM.

References

1. R.H. Rediker, T.A. Lind, and B.E. Burke, "Optical Wavefront Measurement and/or Modification Using Integrated Optics," J. Lightwave Tech., vol. 6, pp. 916-932, 1988.
2. F.J. Leonberger and J.P. Donnelly, "Semiconductor Integrated Optic Devices," in Guided-Wave Optoelectronics, ed. T. Tamir (Berlin: Springer-Verlag, 1988).
3. R.H. Rediker, F.J. Leonberger and D.P. Greenwood, "Method and Apparatus for Processing Optical Wave Signals," U.S. Patent 4,798,437, issues January 17, 1989.
4. R.H. Rediker, T.A. Lind, R.A. Becker and L.M. Johnson, "Design, Fabrication and Characterization of Horn Antennas in Ti-Indiffused LiNbO_3 Channel Waveguides," Tech. Digest 7th Topical Meeting on Integrated and Guided Wave Optics (1984), Optical Society of America, pp. WC4 (1-3).
5. G.E. Mueller and W.A. Tyrell, "Polyrod Antennas," Bell Syst. Tech. J., vol. 26, pp. 837-851, 1947.
6. W.D. Goodhue, J.J. Zayhowski, and K.B. Nichols, "Planar Quantum Wells with Spatially Dependent Thicknesses and Al Content," J. Vac. Sci. Technol. B, vol. 6, pp. 846-848, 1988.
7. W.D. Goodhue, D.E. Bossi, M.C. Finn, J.W. Bales, and R.H. Rediker, "Reduced-Confinement GaAlAs Tapered-Waveguide Antenna Grown by Molecular-Beam Epitaxy," J. Vac. Sci. Technol. B, vol 8, pp. 349-351, 1990.
8. R. Fischer, J. Klem, T.J. Drummond, R.E. Thorne, W. Kopp, H. Morkoc, and A.Y. Cho, "Incorporation Rates of Gallium and Aluminum on GaAs During Molecular Beam Epitaxy at High Substrate Temperatures," J. Appl. Phys., vol. 54, pp. 2508-2510, 1983.

References (Contd)

9. J. Ralston, G.W. Wicks, and L.F. Eastman, "Reflection High-Energy Electron Diffraction Intensity Oscillation Study of Ga Desorption from Molecular Beam Epitaxially Grown $\text{Al}_x\text{Ga}_{1-x}\text{As}$," J. Vac. Sci. Technol. B, vol. 4, pp. 594-597, 1986.
10. E. Kapon and R. Bhat, "Low-Loss Single-Mode GaAs/AlGaAs Optical Waveguides Grown by Organometallic Vapor Phase Epitaxy," Appl. Phys. Lett., vol. 50, pp. 1628-1630, 1987.
11. P.G. Suchoski, Jr. and R.V. Ramaswamy, "Design of Single-Mode Step-Tapered Waveguide Sections," IEEE J. Quantum Electron., vol. QE-23, pp. 205-211, 1987.
12. D. Marcuse, "Radiation Losses of Step-Tapered Channel Waveguides," Appl. Opt., vol. 19, pp. 3676-3681, 1980.